The effect of the orientation of cubical projectiles on the ballistic limit and failure mode of AA2024-T351 sheets

T. De Vuyst[a,*], R. Vignjevic[a], A. Azorin Albero[a,b], K. Hughes[a], J.C. Campbell[a], N. Djordjevic[a]

[a] Structural Integrity, Institute of Materials and Manufacturing, Brunel University London, Granta Park, NSIRC, Great Abington, Cambridge CB21 6AL, UK
[b] Applied Mechanics, SATM, Cranfield University, Cranfield, Bedford, MK43 0AL, UK

ARTICLE INFO

ABSTRACT

This paper presents the results of an investigation of the ballistic limits and failure modes of AA2024-T351 sheets impacted by cubical projectiles. The effect of cube orientation on the ballistic limit and failure modes was considered in detail. Three impact configurations were investigated. Configuration one, two and three considered face, edge or corner impacts correspondingly. The experimental results were complemented with finite element analysis results in order to explain the observations.

The lowest ballistic limit (202 m/s) was observed when the cube edge impacted on the target. In the cube face impacts, the ballistic limit was higher (223 m/s), and the highest ballistic limit (254 m/s) was observed for the corner impact. Although the face impact did not have the lowest ballistic limit, this impact configuration resulted in the least amount of projectile energy loss for impacts above the ballistic limit.

With the aid of finite element modelling, it was possible to develop a better understanding of the test results and explain that the observed differences in impact response were not just due to a difference in projectile frontal area, but also due to the combination of the localised deformation near the projectile impact point and the resulting global (dishing) deformation.

1. Introduction

In the literature on ballistic limit studies, the majority of published works considers cylindrical (rod-shaped) projectiles with a range of nose shapes. The most common types of nose shapes are ogive, flat, conical and hemispherical, as shown in Fig. 1. An overview of published work with impact velocities and projectile and target dimensions that are of the same order as the ones used in this paper is provided in this section.

In 1978 and 1984, Woodward [1,2] published analytical models for the prediction of ballistic limit of metal targets. These models investigate the effect of work done by bending forces on the accuracy of predictions. The models consider ductile hole formation, ductile plugging, adiabatic shear and discing modes of failure and uses the work done to penetrate the target to explain the occurrence of specific modes of failure in terms of projectile shape, target configuration and material properties (including work hardening and thermal softening rates). More recently, Rosenberg and Dekel [3] presented an analytical model for predicting the ballistic limit of ductile plates impacted by ogive and conical nosed projectiles. Their

model distinguishes between dishing and hole enlargement deformation mechanisms.

Apart from analytical models, there are many publications which present experimental results and numerical modelling results for rod shaped penetrators. For example, Gupta et al. studied the ballistic performance of thin AA1100 plates [4−9] and Weldox plates [10] for cylindrical projectiles with different nose shapes. In [4] they also studied the effect of boundary conditions by clamping 1 mm thick AA1100-H12 targets along 25%, 50%, 75% and 100% of their circumference. For these thin targets compared to the projectile diameter of 19 mm, they observed a significant effect on energy absorption but no effect on failure mode. In [9], experiments were performed on 1 mm thick AA1100-H12 targets where the ratio of the target diameter to projectile diameter was varied from 3.6 to 15, and in parallel, simulations in the range of 3.6 to 40 was considered. They concluded that the energy absorbed increased for increasing target to projectile diameter ratios up to a ratio of 10 for blunt, and 25 for ogive nose shapes. For higher ratios the energy absorbed remained roughly constant. The ballistic limit of the AA1100-H12 material was also studied for plates with thicknesses 0.5, 0.71, 1.0 and 1.5 mm subjected to impacts with flat, ogive and hemispherical nosed cylindrical projectiles in [7] and extended to thicknesses of 2.0, 2.5 and 3.0 mm in [8]. Apart from studying the ballistic limit of monolithic
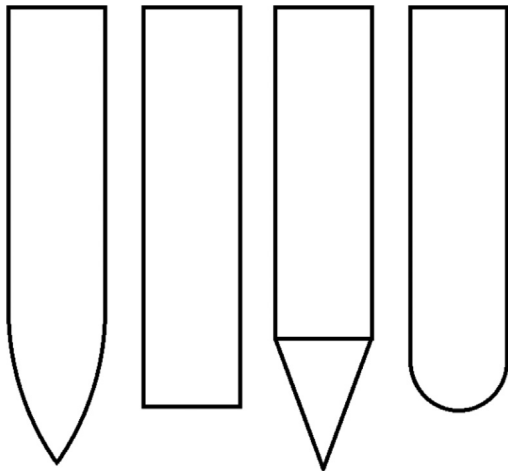
Fig. 1. Common projectile nose shapes, from left to right: Ogive, Blunt/Flat, Conical, Hemispherical.

targets, [7,8] also include a study of the ballistic limit of multi-layered targets in different configurations of number of layers and layer thickness. It was concluded that ogive nosed penetrators required the lowest energy to perforate and plates with more than two layers resulted in lower resistance to penetration than single or two layered plates. In [5] Gupta et al. studied the ballistic performance of 0.82 and 1.82 mm thick AA1100-H14 sheets subjected to impact with double nosed impactors, and Iqbal et al [10] contains a numerical modelling study of the effect of cone angle of conical nosed 20 mm diameter cylindrical projectiles on the ballistic limit of 12 mm thick Weldox 460 E steel. A similar numerical study presented in [6] includes ogive nosed projectiles and 1 mm thick 1100-H12 aluminium targets.

In [11] Senthil and Iqbal studied 1 mm thick monolithic and double-layered plates of 2 stacked 0.5 mm thick sheets made of AA1100-H12 aluminium. In this study, the effect of the target thickness to projectile diameter ratio was investigated. The size of the projectile was varied by varying its shank diameter as 15, 19 and 24 mm. It was concluded that the ballistic resistance increased with increasing projectile diameter, and that the monolithic target offer the highest resistance.

Other authors such as Rusinek et al [12–16] and Borvik et al [17–19] also studied the effect of nose shape of cylindrical projectiles on the ballistic limit of various target configurations. In [12] Rodríguez-Millán, Vaz-Romero, Rusinek, Rodríguez-Martínez and Arias considered the impact of flat, conical and spherical nosed cylinders of diameter 13 mm on 4 mm AA 5754-H111 and AA 6082-T6 plates for velocities ranging from 50 m/s to 200 m/s. The failure mechanisms for both materials are different mainly due to differences in ductility. The ballistic limit for a flat nosed projectile is lower than for the hemispherical and conical nosed impactors. It was concluded that the energy absorption is dependent on the combination of the following factors: target material behaviour, projectile nose shape and impact velocity. Jankowiak, Rusinek, and Wood [13] performed a numerical study of 2 mm and 4 mm monolithic and layered sheets impacted by conical, hemispherical and flat nosed cylindrical projectiles with 13 mm diameter and 26 mm length. The influence of material, projectile mass and effect of friction was discussed. These authors concluded that the target thickness was the most important parameter affecting ballistic limit and also concluded that monolithic targets were more efficient than multilayer targets.

In [14] Rusinek, Rodríguez-Martínez, Arias, Klepaczko and López-Puente studied the effect of projectile diameter of a conical nosed projectile impacting a Weldox 460 E steel 12 mm thick plate. The ballistic limit increased linearly with projectile diameter. In [15], this was extended by a numerical study of 20 mm diameter blunt,

conical and hemispherical nosed projectiles impacting Weldox 460 E of 12 mm thickness. The authors concluded that the blunt nosed projectile resulted in the lowest ballistic limit. The same material was studied in [16]. Borvik, Hopperstad and Pedersen studied the impact of blunt and ogive 20 mm diameter steel cylinders on AA7075-T651 sheets of thickness 20 mm in [17]. The target failure mode is brittle, with fragmentation and delamination failures observed. Borvik, Dey and Clausen [18] investigated the perforation resistance of five different high-strength steel plates subjected to small-arms projectiles, and in [19], Borvik et al also studied the impact of 20 mm diameter ogive nosed projectiles on AA6005-T6 extrusions with 6 mm front and back thickness and total depth of 130 mm. Raguraman, Jagadeesh, Deb and Barton [20] studied the impact of conical, ogive, hemispherical and blunt nosed steel cylinders with a diameter of 15 mm on 1 mm thick 1100 aluminium.

Apart from the literature on cylindrical projectiles with the commonly used projectile nose shapes shown in Fig. 1, there have also been some studies on the ballistic response to more complex nose shapes such as "dualnose" [15,16] and "shrapnel" type projectiles [21]. Another aspect of ballistic resistance which has received attention from authors such as Yunfei et al [22–25], Deng, Zhang and Cao [26,27], Jankowiak, Rusinek and Wood [13], Woodward and Cimpoeru [28] is the use of multi-layered targets, where targets are an assembly of two or more sheets. These multi-layered targets sometimes include a stand-off distance (or air gap) between the sheets, but in other cases the sheets are simply stacked together (no air gap).

From the papers listed above, the projectile aspect ratio (length to diameter) for cylindrical projectiles was roughly in the range of 2 to 5. Apart from these rod shaped impactors, other authors considered impactors with an aspect ratio close to one. Erice [29] for example considered the impact of 5.55 mm diameter steel spherical projectiles on 1.6 mm thick Inconel 718 plates. The tests were conducted at three different temperatures, and for velocities between 300 m/s and 800 m/s. A study by Seidt et al [30] on AA2024-T3 targets impacted by steel and titanium projectiles demonstrated that the material anisotropy had significant effect on the predicted residual velocity of the projectile. In [31], Wang and Zhou studied the penetration of 5 mm thick explosively welded steel/aluminium plates when subjected to impacts by cylindrical (diameter 6 mm) and cubical (length 4.2 mm) projectiles. The ballistic limit was lower for the spherical projectile. However, the cubical projectiles were noticeably deformed by hitting the target face on. Jordan [21] studied a range of compact fragments, fragments with an L/D ratio in the range 0.9 - 1.3, on glass fibre reinforced plastic (GFRP) targets with sheet thicknesses of 4, 9 and 14 mm. The mass for all fragments was kept constant, and the parameters varied include nose shape, target thickness and impact velocity. Ulven, Vaidya, Hosur [32] studied hemispherical, flat and conical nosed cylindrical projectiles with aspect ratio close to one but the targets used in their research were carbon/epoxy laminates of 6.5 and 3.2 mm thickness. Similarly Tan, Lim and Cheong [33] also considered hemispherical, ogive, flat and conical nosed cylindrical projectiles with aspect ratio close to one using for targets manufactured from aramid fibre fabric sheets.

The objective of the work presented in this paper was to investigate the effect of cubical projectile orientation on the ballistic limit. In order to achieve this, a number of ballistic impact experiments and finite element analyses with cubical projectiles were performed. The cube impact tests were performed for three different cube orientations leading to three impact configurations: face, edge and corner as shown in Fig. 2. The observed differences in ballistic limit

Fig. 2. Impact configurations considered: a) cube face, b) cube edge, c) cube corner.
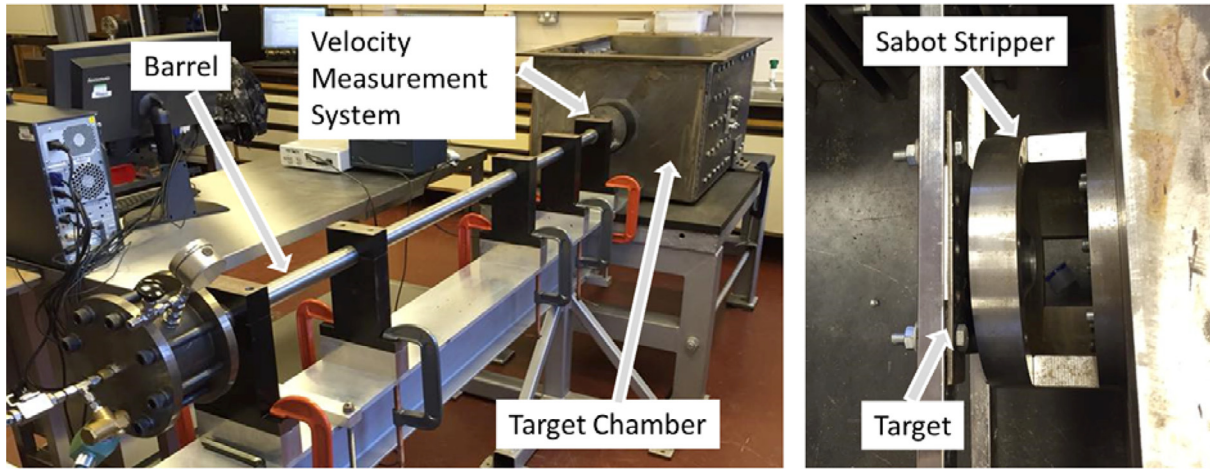
Fig. 3. Experimental Setup.

are explained in terms of differences in failure mode for the different impact configurations. Furthermore, the observations are complemented by numerical simulations which allow a more detailed interpretation of the experimental observations.

2. Experiments

2.1. Description

The series of impact tests were performed against AA2024-T351 sheets with a thickness of 3.175 mm. Cubical projectiles with an edge

Table 1
Summary of impact and residual velocities for experiments, FE simulations and Recht-Ipson equation.

Projectile	v i [m/s]	v r exp [m/s]	v r sim [m/s]	v r analyt [m/s]
Face	221	0	0	0
Face	226	72	0	76
Face	240	144	106	127
Face	279	184	188	198
Face	321	251	234	252
Edge	198	0	0	0
Edge	215	47	41	54
Edge	231	100	87	88
Edge	272	155	152	153
Edge	303	189	182	196
Corner	249	0	0	0
Corner	263	47	30	48
Corner	290	111	104	110
Corner	324	167	169	168

length of 9.5 mm and mass of 6.9 g were used. The target plates were clamped at two opposite edges, leaving the other two edges free. The unclamped area of the targets was 120 mm x 120 mm (see Fig. 3). The projectiles were accelerated using a single stage gas gun (see Fig. 3). The barrel had a length of 2 m and at maximum pressure, accelerated projectiles to velocities of around 325 m/s. The projectile velocity was measured using an optical velocity measurement system consisting of two light beams and photodiodes. The time interval between the projectile interrupting the two light beams allowed for the velocity of the projectile to be calculated. The projectiles were placed in a sabot for launch, and in order to ensure the desired projectile orientation at impact, the free flight distance was reduced by locating the target close to the sabot stripper (50 mm separation). The high speed camera images of the experiments were obtained with an Olympus i-SPEED 3 high speed camera recording at 30,000fps.

2.2. Overview of experimental results

The impact and residual velocities from the experiments are summarised in Table 1 and a plot of residual velocity versus impact

Table 2
Summary of parameters for the Recht-Ipson equation.

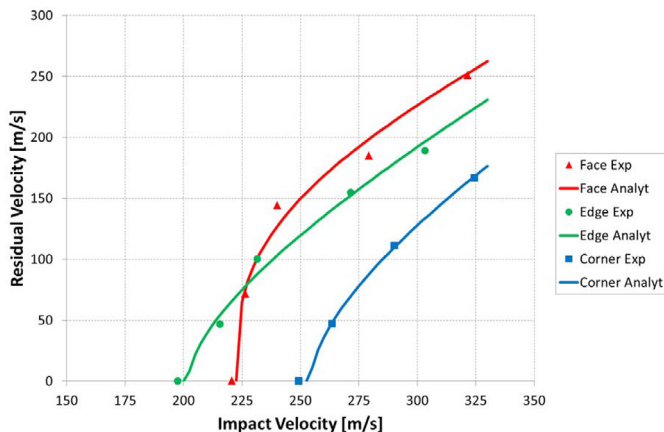| Type	Ballistic Limit [m/s]	p	A
Face	223	3.0	0.90
Edge	202	1.6	1.00
Corner	254	1.7	1.00

Fig. 4. Ballistic limit curve and Recht-Ipson equation for the three impact configurations.
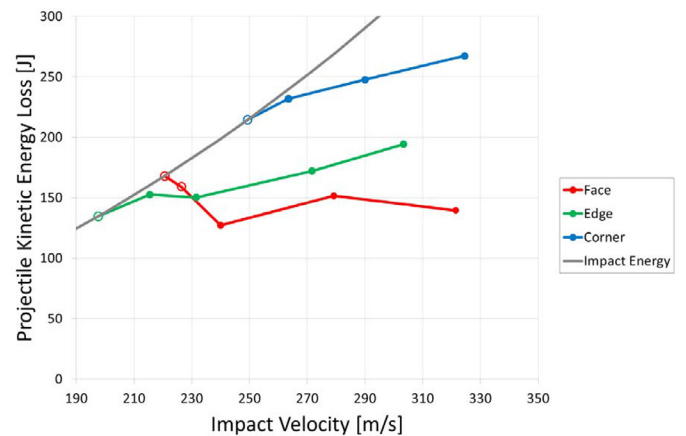

Fig. 5. Kinetic energy loss of the projectile versus impact velocity for the three impact configurations.
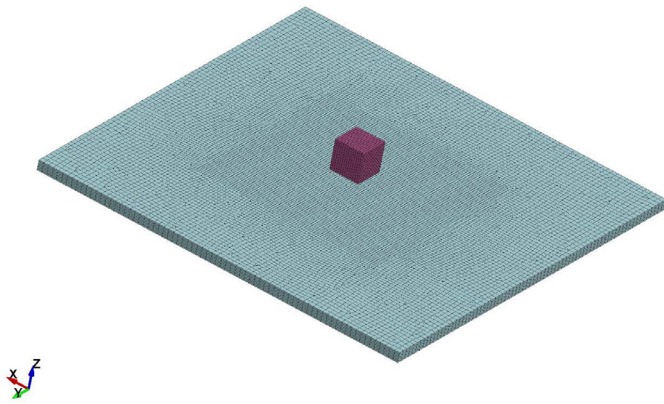
Fig. 6. Finite element model initial configuration.

Table 3
Steel cube material model parameters [37].

Material	Density [kg/m³]	Young's modulus [GPa]	Poisson's ratio [-]	Yield stress [MPa]
Steel	7740	206.8	0.33	470

Table 4
Sets of parameters used for Barlat's six-component anisotropic plasticity model [30].

Parameter set	m	a	b	c	f	g	H
Anisotropic	8	1.378	1.044	0.955	1.0	1.0	1.210
Isotropic	2	1.0	1.0	1.0	1.0	1.0	1.0

velocity is shown in Fig. 4. The ballistic limit was calculated by adjusting the parameters a and p of a Recht-Ipson [34,18] equation applied to the experimental data.

$$v_r = a\left(v_i^p - v_{bl}^p\right)^{1/p}$$

Where

$$a = \frac{m_{projectile}}{m_{projectile} + m_{plug}}$$

The parameters v_{bl} (the ballistic limit) and parameter p were varied to minimise the RMS error between experimental data and the values predicted by the analytical model, the resulting curves are shown with the experimental data points in Fig. 2, and the parameters used listed in Table 2. It can be seen that the ballistic limit for the cube edge impact is the lowest at 202 m/s and the cube corner impact is the highest at 254 m/s. The ballistic limit for cube face impacts is 223 m/s. In other words, there is a 25% variation in ballistic limit depending on projectile orientation.
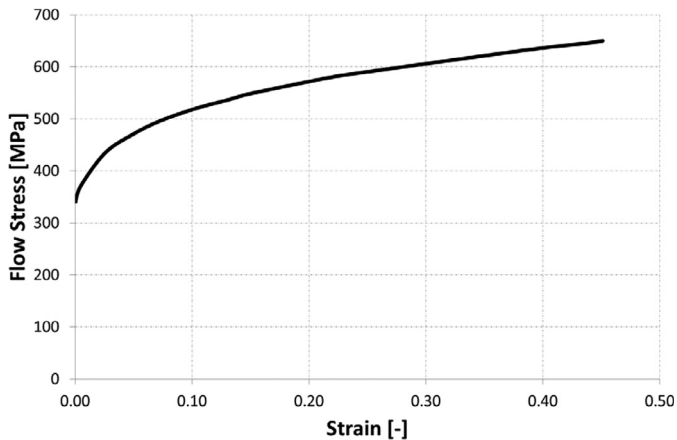

Fig. 7. Evolution of flow stress as a function of effective plastic strain [30].
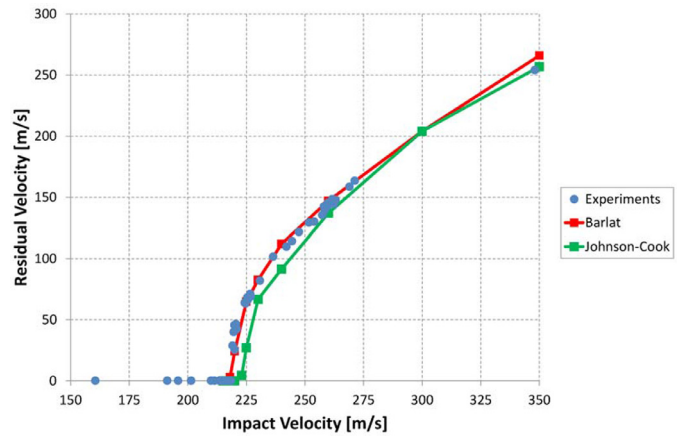

Fig. 8. Comparison ballistic limit curves using Barlat and Johnson-Cook material model for impact experiments on 3.175 mm thick AA2024-T351 in [40].
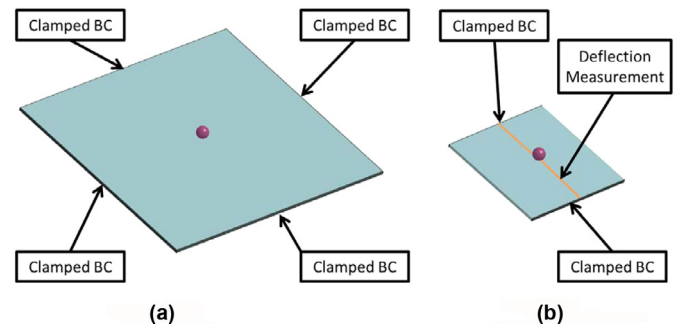

Fig. 9. AA2024-T351 target finite element models a) 250 mm x 250 mm fully restrained b) 120 mm × 120 mm only two sides restrained.
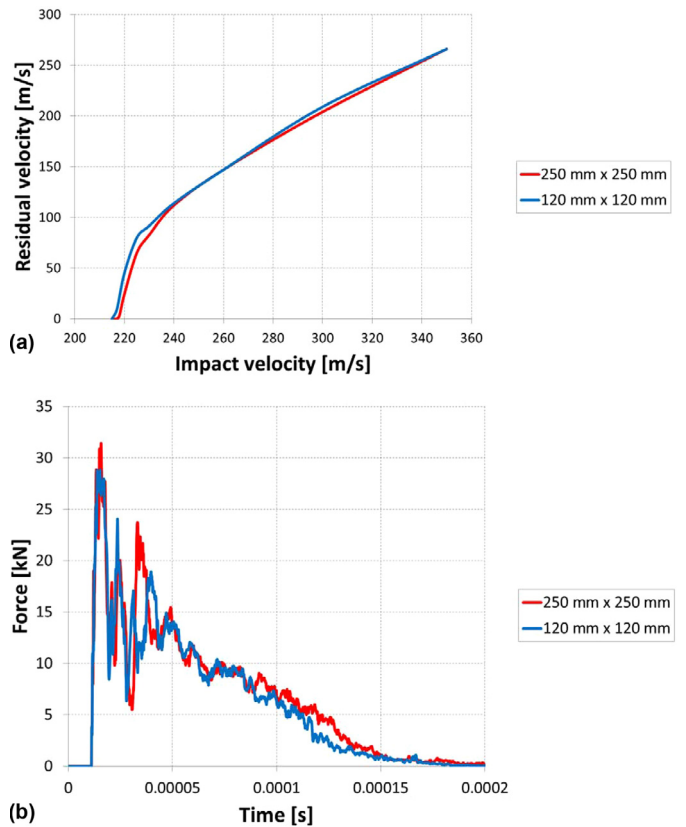

Fig. 10. Sensitivity study of the target size and boundary conditions, a) difference in ballistic limit curves, b) comparison of contact force for impact velocity of 225 m/s.
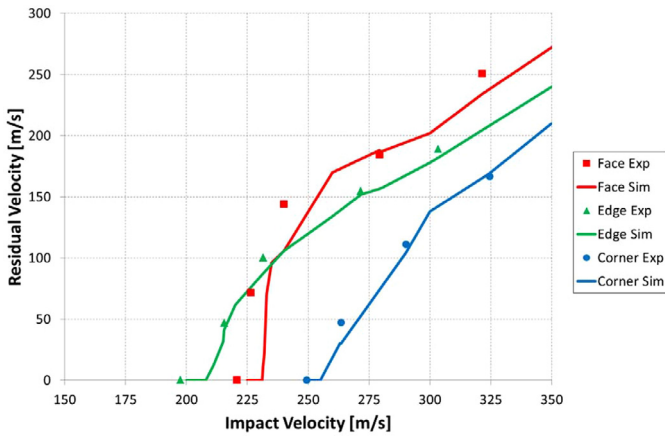
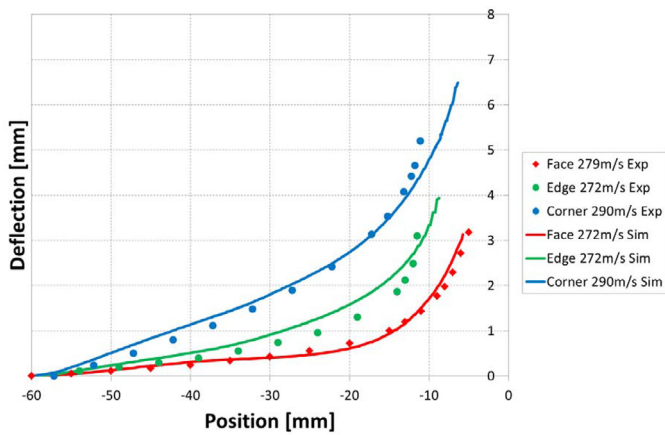**Fig. 11.** Comparison of experimental and simulated ballistic limit curve.

Fig. 12. Comparison of measured and simulated target deflections along the centre of the target in the direction of the clamping for impact velocities around 275 m/s.

Fig. 5 shows the projectile kinetic energy loss as a function of impact velocity. The points with hollow markers are associated with impacts below the ballistic limit. Fig. 5 shows that for the velocity range studied, the energy loss increased with impact velocity for the edge and corner impacts. The face impact case was different. In the case of a face impact below the ballistic limit, the energy loss of the projectile was higher than for the edge impact at the same velocity. However, once the ballistic limit was reached, the face impact

resulted in lower projectile energy loss than the corresponding edge impact.

3. Finite element modelling

The interpretation of the experimental results was aided by a numerical study using the LS-Dyna explicit finite element code [35]. The models were built in Hypermesh [36]. Both projectile and target were modelled with solid elements. The element size was 0.7 mm in the projectile. For the target, seven elements were defined through the thickness of the plate and an element size of 0.8 mm was used at the impact location, coarsening to 1.6 mm in the rest of the target, see Fig. 6. The interaction between target and projectile was modelled with an eroding single surface contact algorithm available in LS-Dyna.

3.1. Material models

The projectile behaviour was modelled using material properties of steel listed in Table 3.

Regarding the model used for the target the parameters were taken from Seidt et al [30], who analysed the ballistic impact of 3.175 mm thick AA2024-T3 sheets using anisotropic material models for the target. They carried out simulations of impact experiments in LS-Dyna using cylindrical projectiles and considered Barlat's six-component anisotropic plasticity model [38] for the aluminium sheet. They used two different sets of parameters for the model, one taking into account the anisotropic plastic response of the target and the other one representing an isotropic (von Mises) yield function, see Table 4.

They observed that the yield function parameters used in the simulations had a significant effect on both predicted ballistic limit and residual velocity of the projectile. Furthermore, they found that the experimental results for the 3.175 mm thick aluminium sheet were predicted more accurately with an anisotropic model. Therefore it was decided in this paper to use the same Barlat anisotropic plasticity material model used by Seidt. This six parameter model uses an associative flow rule:

$$\dot{\epsilon}_{ij} = \lambda \frac{\partial f}{\partial \sigma_{ij}}$$

and yield function:

$$f = \overline{\sigma} - \sigma_{flow}(\overline{\epsilon}^p)$$

and $\overline{\sigma}$ is the equivalent stress [30] which is defined as:

$$2\overline{\sigma}^m = \left| S_1 - S_2 \right|^m + \left| S_2 - S_3 \right|^m + \left| S_3 - S_1 \right|^m$$
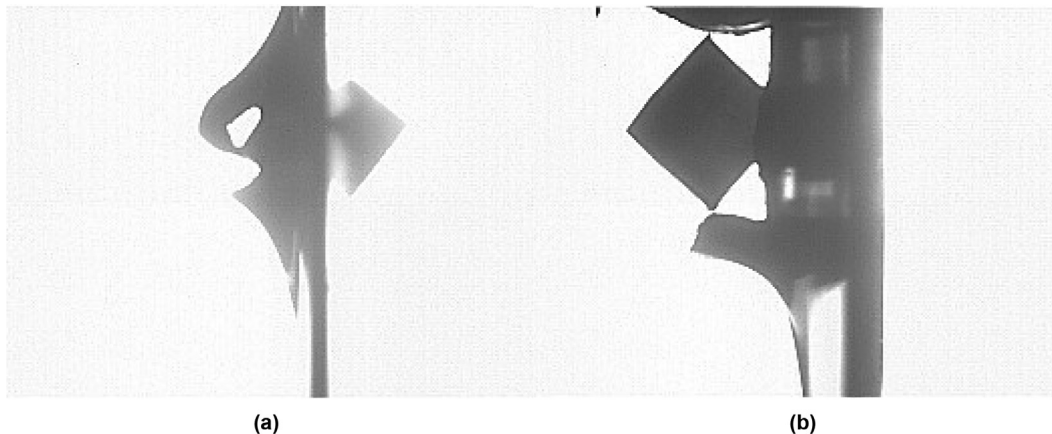

Fig. 13. Edge impact high speed camera images for impact speed of 272 m/s (projectile travels from right to left) a) initial fracture developed, b) complete penetration.

where S_1, S_2 and S_3 are the principal values of the symmetric matrix S with components

$$S_{xx} = [c(\sigma_{xx} - \sigma_{yy}) - b(\sigma_{zz} - \sigma_{xx})]/3$$

$$S_{yy} = [a(\sigma_{yy} - \sigma_{zz}) - c(\sigma_{xx} - \sigma_{yy})]/3$$

$$S_{zz} = [b(\sigma_{zz} - \sigma_{xx}) - a(\sigma_{yy} - \sigma_{zz})]/3$$

$$S_{yz} = f\sigma_{yz}$$

$$S_{zx} = g\sigma_{zx}$$

$$S_{xy} = h\sigma_{xy}$$

and a, b, c, f, g and h are the six parameters required to describe the shape of the yield surface. The hardening was accounted for by defining the flow stress as a function of effective plastic strain, $\sigma_{flow}(\bar{\epsilon}^p)$ in tabulated form (see Fig. 7). The data was obtained from [30].

The Young's modulus (73.084 GPa), density (2770 kg/m³) and the yield function parameters a, b, c, f, g and h accounting for anisotropic response were the parameters Barlat et al [38] identified for the case of an AA2024-T3 sheet (see Table 4). The stress-strain curve defining plastic hardening was taken from a uniaxial compression test carried out on a specimen aligned in the rolling direction of a 12.7 mm thick AA2024-T351 plate in [30]. In this material model, failure can only be modelled through a maximum principal strain at failure element erosion criterion available in LS-Dyna. A value of 0.165 was used in
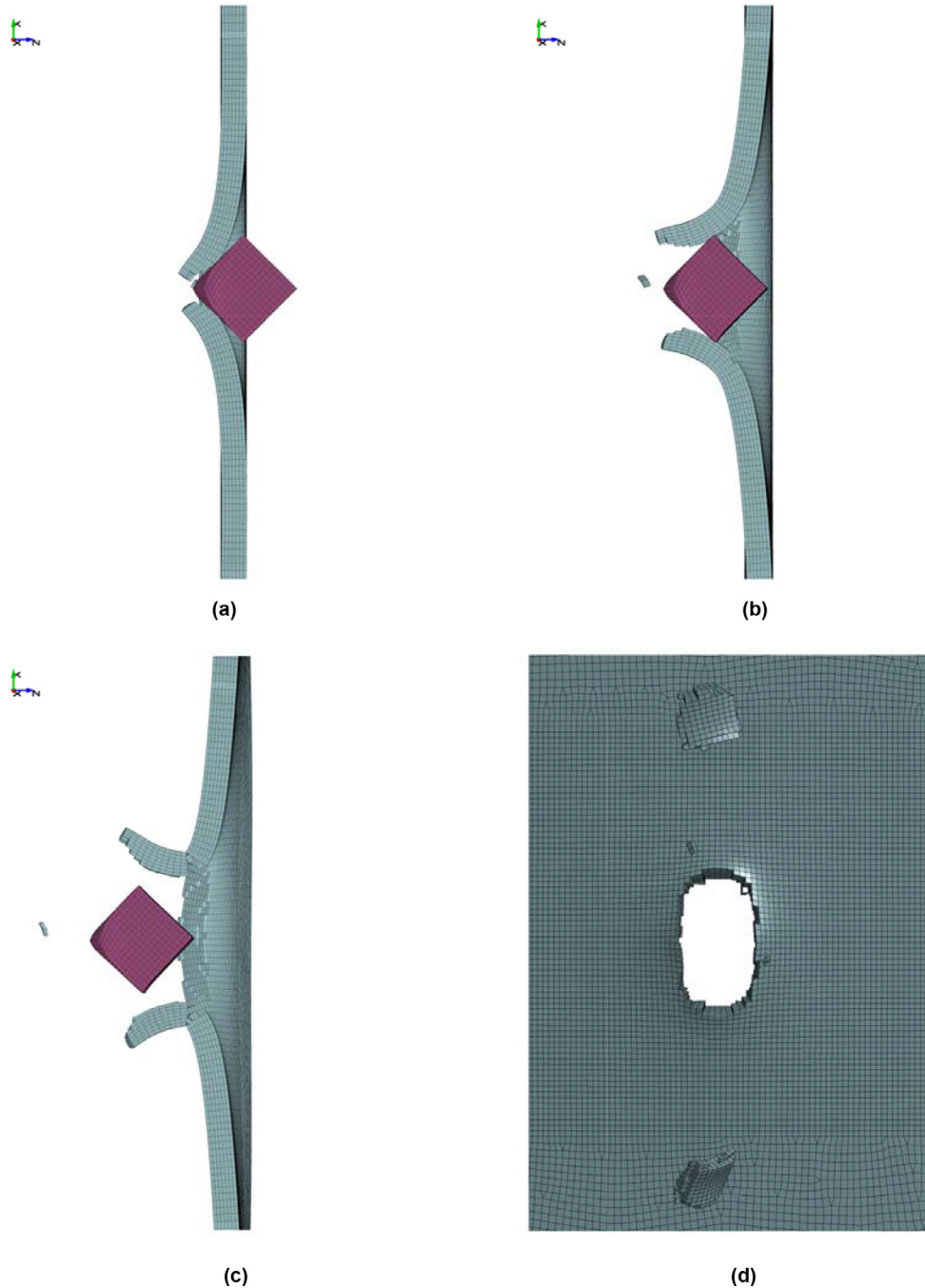

Fig. 14. Edge impact simulation results for impact speed of 272 m/s a) initial fracture developed, b) formation of petals, c) break-off of petals, d) top view showing elliptical hole and petals completely separated.
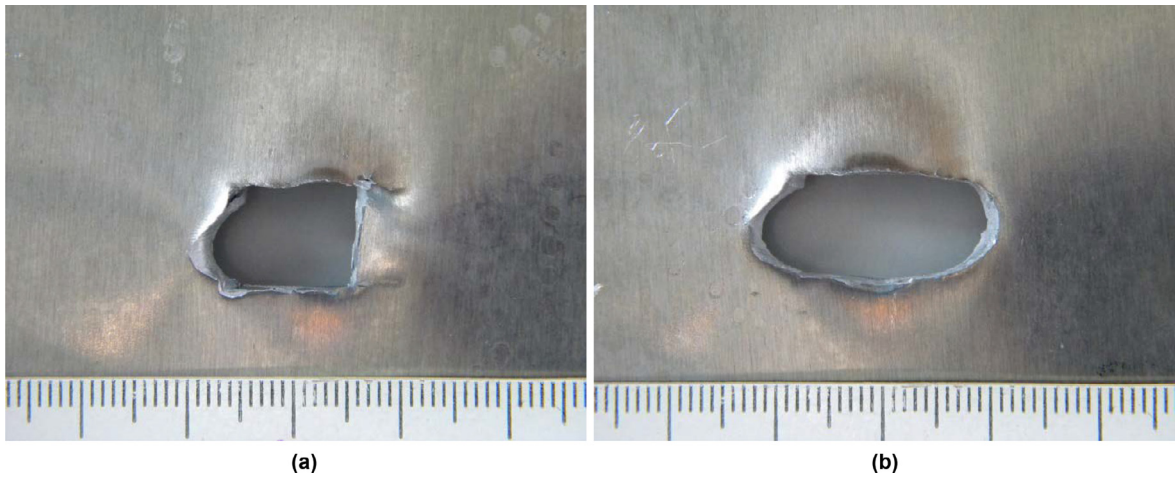
Fig. 15. Edge impact deformed state for impact velocity of a) 215 m/s and b) 303 m/s.

this paper. This value was based on experimental data used in a previous study [39] of the impact experiments reported by Kelley and Johnson [40]. These experiments consisted of a 12.7 mm diameter sphere impacting a 250 mm by 250 mm 3.175 mm thick AA2024-T351 plate clamped around its edges. In the numerical analysis the experiments were first modelled using a Johnson-Cook material and damage model which accounts for the effect of stress triaxiality, strain rate and temperature on failure. The ballistic limit curves using the Johnson-cook and Barlat model, shown in Fig. 8, are in line with Seidt's observations [30] that for this type of impact configuration the use of the Barlat anisotropic plasticity model results in a better prediction of ballistic limit and residual velocity close to the ballistic limit than the Johnson-cook model. This would indicate that in this case the accurate description of energy absorption through yield surface and material hardening is more important than damage, which includes stress triaxiality and material failure.

3.2. Effect of boundary conditions

In many impact experiments on thin targets reported in this literature review, the targets were fully clamped around their circumference. The study of the effect of boundary conditions on circular targets performed in [4] showed that the observed behaviour was dependent on boundary conditions. Therefore, the influence of boundary conditions and target size was assessed by performing a sensitivity analysis based on the tests reported in Kelley and Johnson [40]. This sensitivity analysis consisted of the impact of a 12.7 mm diameter steel sphere against two different sized aluminium targets. The first target was 250 mm x 250 mm in size and had the four edges fully clamped; the second target was 120 mm x 120 mm in size and had two opposite edges fully restrained. Both of them were modelled with Barlat's material model. Fig. 9 shows the two different finite element models used for comparison of results.

The simulation results obtained with these models are presented in Fig. 10, where residual velocities and the contact force data are shown.

It can be observed that the different dimensions and boundary conditions do not show a significant effect on the target behaviour under ballistic impact conditions with a spherical projectile. The contact force history curves obtained are very similar, and this similarity was corroborated by the small differences in ballistic limit and residual velocities observed (see Fig. 10).

3.3. Overview of FEA results

The residual velocities obtained by the finite element modelling are summarised in Table 1. It can be seen that the finite element

results correlate well with the experimental data for each of the impact configurations considered. This is illustrated in Fig. 11 where the ballistic limit curves for experiment and simulation results for the three impact configurations are compared. The L^2 relative error norms are 0.24, 0.06 and 0.09 for the face, edge and corner impact configurations respectively. The plate deflections (along the centre of the plate in the direction of the clamping, see Fig. 9b) are compared for an impact velocity around 275 m/s in
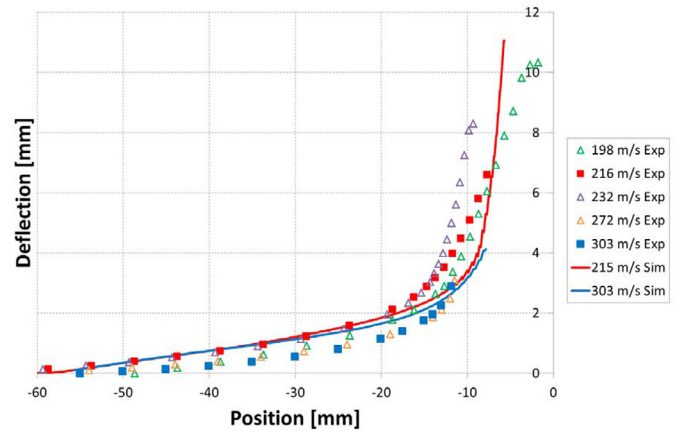

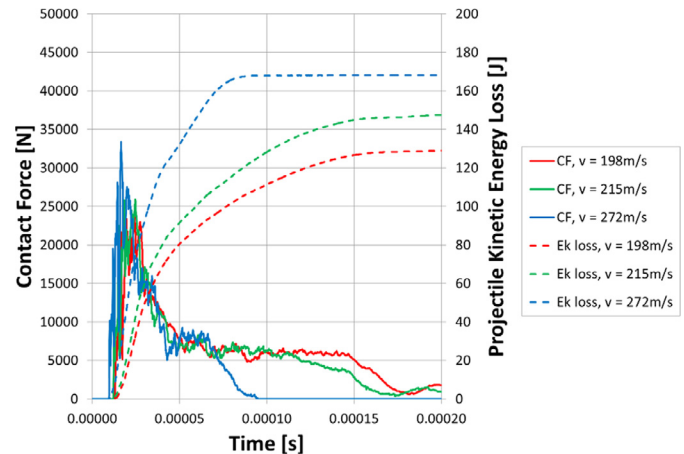**Fig. 16.** Edge impact global deformation as a function of impact speed.

Fig. 17. Edge impact contact force and projectile kinetic energy loss as a function of time. The 198 m/s impact is below the ballistic limit, the 215 m/s and 272 m/s impacts are above the ballistic limit.
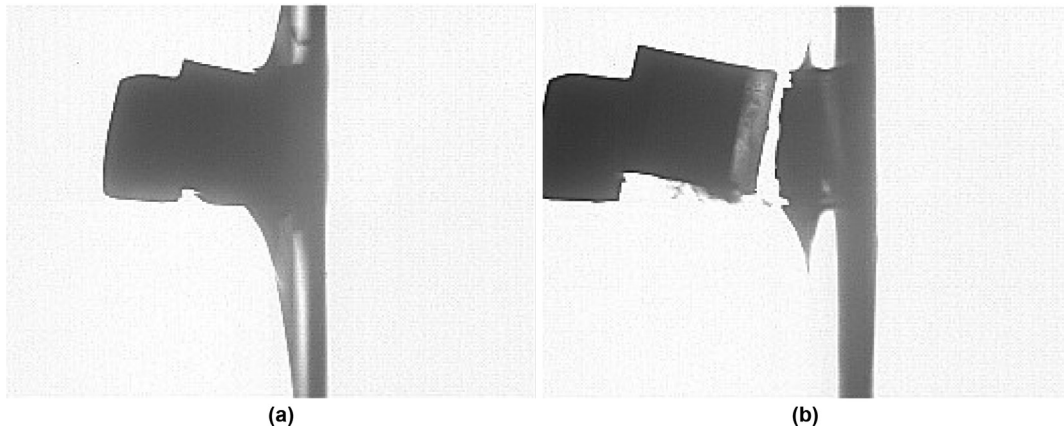
Fig. 18. Face impact high speed camera images for impact speed of 279 m/s (projectile travels from right to left) a) plug fully developed, b) complete penetration.
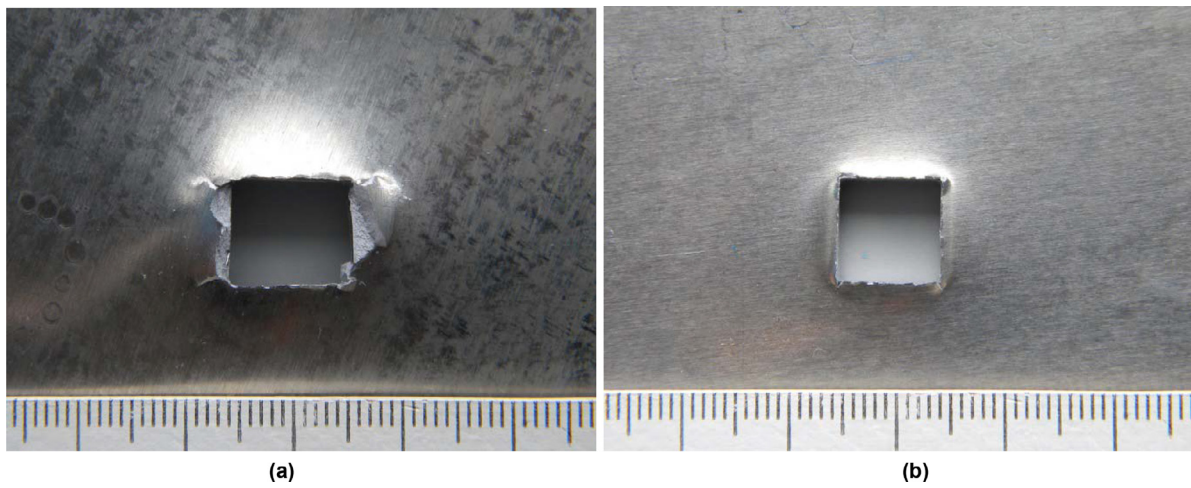

Fig. 19. Face impact deformed state for impact velocity of a) 226 m/s and b) 321 m/s.

Fig. 12. The deflections obtained from the finite element model match the experimentally measured deflection reasonably well. The L^2 relative error norms for the deflections are 0.10, 0.33 and 0.18 for the face, edge and corner impact configurations respectively. It can be noticed that the amount of dishing varies significantly depending on impact configuration. At 275 m/s, y, the face impact shows the least amount of dishing, and corner impact the highest amount. In the next sections, each impact configuration will be described in more detail.
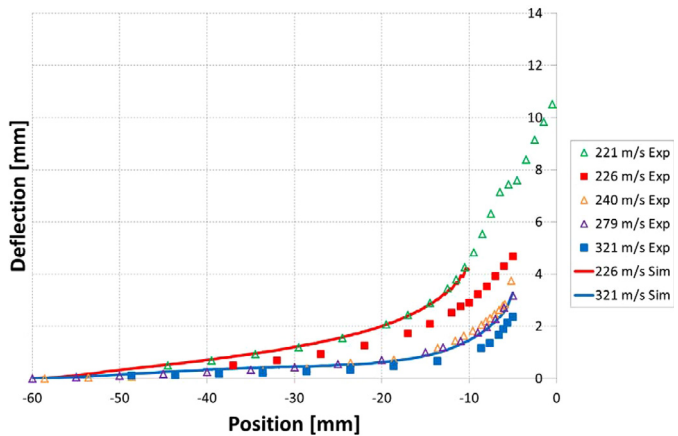

Fig. 20. Face impact global deformation as a function of impact speed.

4. Detailed results

4.1. Edge impact results

The edge impact configuration resulted in the lowest ballistic limit. For this configuration, the penetration mechanism con-
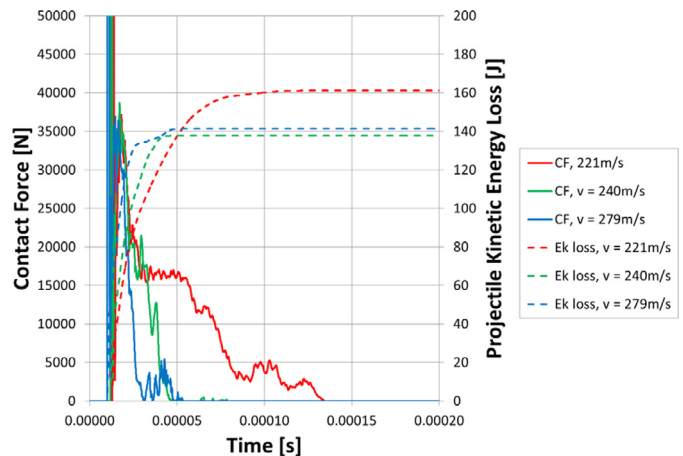

Fig. 21. Face impact contact force (CF) and projectile kinetic energy loss (Ek loss) as a function of time. The 221 m/s impact is below the ballistic limit, the 240 m/s and 279 m/s impacts above the ballistic limit.

sisted of rapid localised deformation around the edge contact area, and as deformation in this area increased, ductile fracture occurred in the vicinity, see Fig. 13. Once the initial fracture developed, the penetration continued through crack growth and bending of the resulting petals as shown on the high speed images in Fig. 13 and simulation results in Fig. 14. The resistance offered by the petals was such that projectile momentum continued to be transferred to the target resulting in dishing of the target. The initial fracture/perforation was generated with relatively little loss in kinetic energy of the projectile. No plug formation was observed for this impact configuration.

As the impact velocity increases these petals bend so far that one or both of the petals break off (see Fig. 15), leaving an elliptical shaped hole. For the 215 m/s impact, one of the petals detached (see Fig. 15a) and the dimensions of the principal axes of the hole are 9.7 and 13.8 mm. The simulation predicts 11.7 and 9.8 mm, but both petals remained attached in the simulation (if one petal is ignored, the dimension would be 11.7 and 16.7 mm). In the case of the 303 m/s impact, both petals break off (see Fig. 15b) and the

dimension of the principal axes are 9.7 and 21.2 mm, whilst the simulation predicts 11.0 and 18.4 mm. Due to the increasing level of bending and separation of the petals, the hole diameter does vary significantly with impact speed, implying a larger amount of energy absorbed at higher impact speeds.

The amount of dishing deceased with increasing impact speed. The simulation results for the amount of dishing are closer together than the ones observed in the experiments (see Fig. 16). The contact force plots in Fig. 17 show that for higher impact speeds the interaction time of the target with the projectile at an impact speed of 275 m/s was about half the time of the impact speed at 215 m/s, which is just above the ballistic limit. This shorter interaction leads to less energy being absorbed by dishing at higher impact speeds.

Overall, the energy absorbed increases with impact velocity, as can be seen in Figs. 5 and 17. This implies that the increase in energy absorbed through the formation and breaking of petals increases faster with increasing impact speed and has a greater effect than the reduction in energy absorbed through dishing.
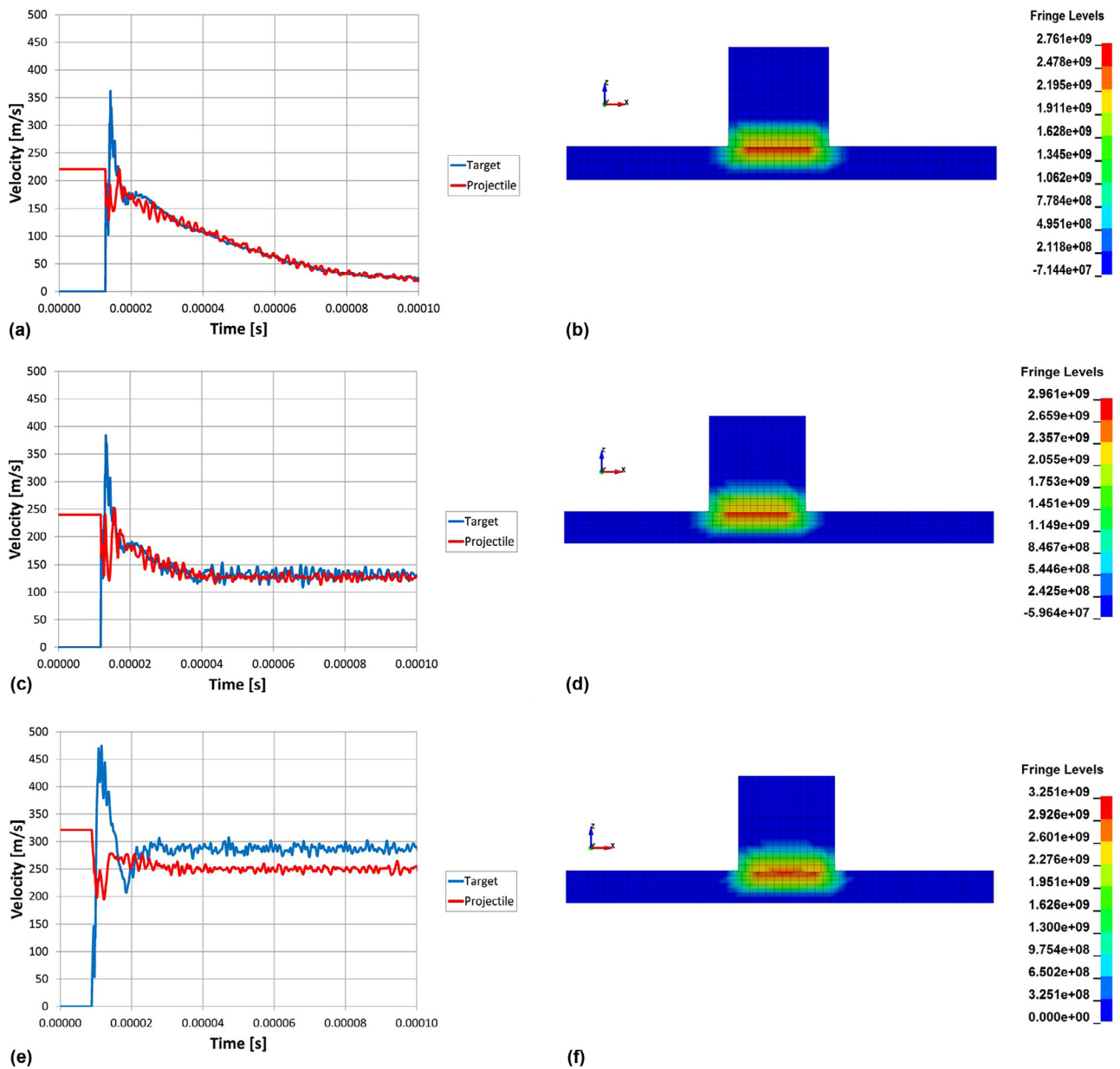

Fig. 22. Velocity time histories of node in projectile and target for impact speed a) 220 m/s, c) 240 m/s and e) 321 m/s, and Peak Pressure [Pa] for impact speed b) 220 m/s, d) 240 m/s and f) 321 m/s.

4.2. Face impact results

The failure mode for the face impact configuration was mainly plugging as shown in the high speed pictures in Fig. 18.

In Fig. 19, the deformed state for impact velocities of 226 m/s and 321 m/s are shown. The impact velocity of 226 m/s is the lowest impact velocity resulting in penetration, while the impact velocity of 321 m/s is the highest tested. The variation in hole dimension was very small over the velocity range tested, with 9.6 by 9.6 mm measured for the 226 m/s impact versus 9.8 by 9.8 mm for the 321 m/s impact.

In comparison with the edge impact, there is less dishing of the target except for the impact test at 221 m/s which did not result in penetration and shows similar levels of dishing as the corresponding edge impact (see Fig. 20). The contact force time history plots in Fig. 21 illustrate this further. There is, as expected, a large peak when contact first occurs which is in the region of 200−250 kN. This force peak is not visible in Fig. 21 as it is outside the range shown. For the impact velocity of 221 m/s, which is below the ballistic limit, the initial peak is followed by a period where the contact force remains constant at the level of around 15 kN and results in a significant reduction in projectile kinetic energy.

For higher impact velocities above the ballistic limit, the initial momentum transfer to the target is such that a plug is formed and the contact force drops to zero immediately after the plugging. At this point, there is no further momentum transfer to the target, as can be seen in the projectile energy loss time history curves in Fig. 21. This also explains the reduced level of dishing for impacts above the ballistic limit. This is in agreement with Backman and Goldsmith [41], who state that in many experiments, dishing deformation delays penetration and increases the ballistic limit. The second peak in the contact force for the 279 m/s test is due to the projectile coming into contact with the edge of the hole created by the ejection of the plug.

The maximum out of plane deflection decreases with impact speed increase (see Fig. 20). The deflection at 226 m/s was 4.2 mm and the deflection at 321 m/s was 2.4 mm, with the simulations predicting similar deflections of 4.2 and 3.3 mm respectively.

The energy absorbed drops just above the ballistic limit and then remains relatively constant, as shown in Figs. 21 and 5.

4.2.1. Plug formation and dishing mechanisms

A further insight into the mechanisms resulting in plug formation and dishing can be gained by looking at finite element plots of the velocity component in the impact direction for two nodes; one lying close to the impact surface inside the projectile and the other close to the impact surface but within the target. In Fig. 22a, it can be seen that for an impact velocity below the ballistic limit, the velocities of these two points reach the same velocity (equilibrium) within a time interval of less than 10μs. Following this stage, the projectile
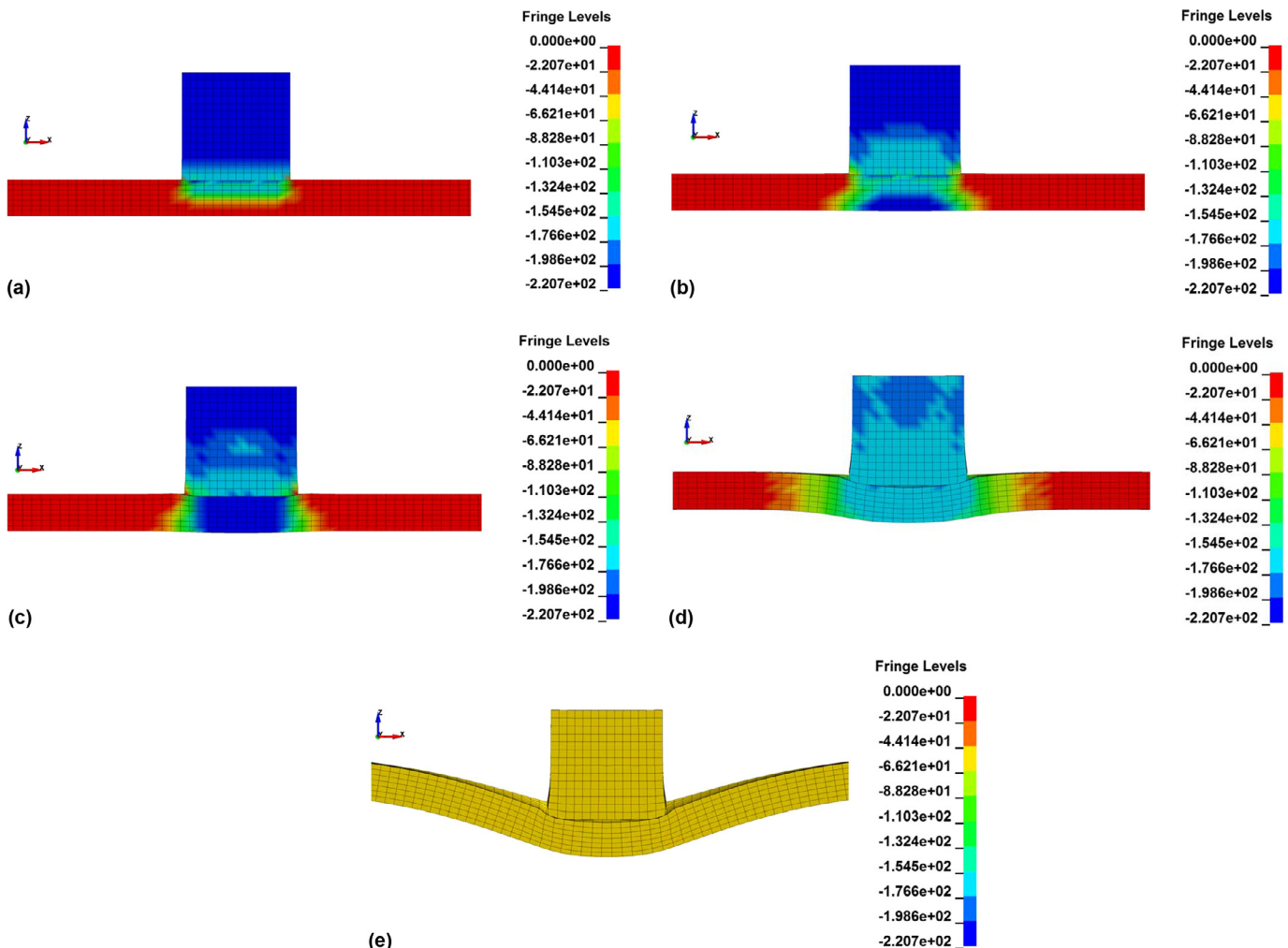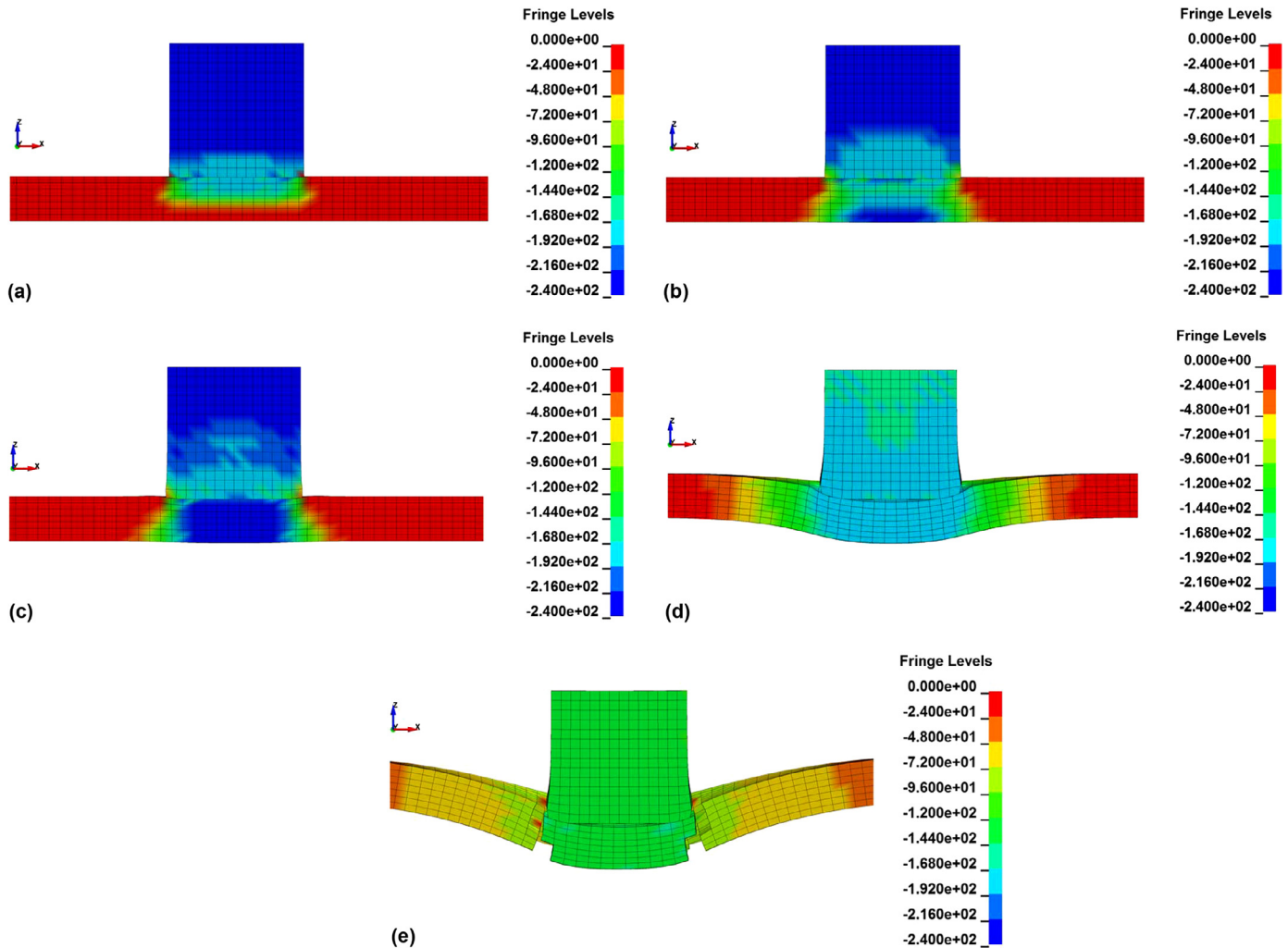

Fig. 23. Velocity in impact direction for 220 m/s impact a) immediately after contact (t = 13.188us), b) when release wave travels from back of target (t = 13.586us), c) when release wave has completely released the target (t = 13.985us), d) when target and projectile are in equilibrium travelling at the same speed (19.299us), e) when the target has slowed down the projectile and resulting dishing deformation is clearly present (t = 62.488us).

Fig. 24. Velocity in impact direction for 240 m/s impact a) immediately after impact (t = 12.179us), b) when release wave travels from back of target (t = 12.484us), c) when release wave has completely released the target (t = 12.882us), when target and projectile are in equilibrium travelling at the same speed (21.584us), when the target has generated a plug (t = 43.183us).

and target gradually slow down and eventually the projectile is brought to rest completely without resulting in perforation of the target. If the impact velocity is increased to just above the ballistic limit (see Fig. 22c), the behaviour was similar, i.e. after initial equilibrium has been reached the projectile and target material slow down at the same rate. This continues until a plug has been formed approximately 25μs after impact. At this point, the projectile and plug continue to move with roughly equal speed. If the impact speed is increased further, such the 321 m/s case shown in Fig. 22e, a plug is formed before initial equilibrium has been reached, and there is noticeable difference in the velocity of plug and residual velocity of the projectile.

This can be further explained by first noting that due to two flat surfaces coming into contact, very high pressures in the range of 3 GPa are generated (see Fig. 22b, d and f) at the contact surface. This will cause a pressure wave to travel into the target and projectile. This is clearly visible from the velocity plots of a cross section midway through projectile and target in Figs. 23–25 for the cases below the ballistic limit (220 m/s) and above the ballistic limit (240 m/s and 321 m/s) respectively. In each of these figures, plot a) shows the wave travelling into the target, b) reflecting of the target back surface and c) unloading the target material below the projectile.

Considering an impact below the ballistic limit (at 220 m/s), one can observe that following this initial wave propagation, no failure

was initiated and the residual momentum is transferred through a gradual reduction in velocity, resulting in dishing of the target (Fig. 23d and e). When the velocity is increased to 240 m/s (Fig. 24), then following the initial wave propagation, the residual momentum results in the simultaneous development of a plug and dishing deformation. The amount of dishing is lower than if the impact velocity is below the ballistic limit. Finally at 321 m/s (see Fig. 25), the generation of a plug starts (Fig. 25d) when the release wave unloading the target material has just entered the projectile. Therefore, the plug velocity is in this case the result of a wave propagation effect rather than a gradual straining of material at lower speeds.

4.3. Corner impact results

In the case of the corner impact configuration, the failure mechanism is similar to the edge impact configuration. First, cracks appear through tensile failure around the impact point, which results in ejection of a small triangular fragment which can be seen in Fig. 26a. From this initial perforation, three cracks (corresponding to the edges which intersect at the impact corner) then propagate, resulting in the formation of three petals. As the projectile advances, these petals bend and become larger and in some cases detach, as shown in Figs. 27 and 28. Furthermore, it is important to note that in this
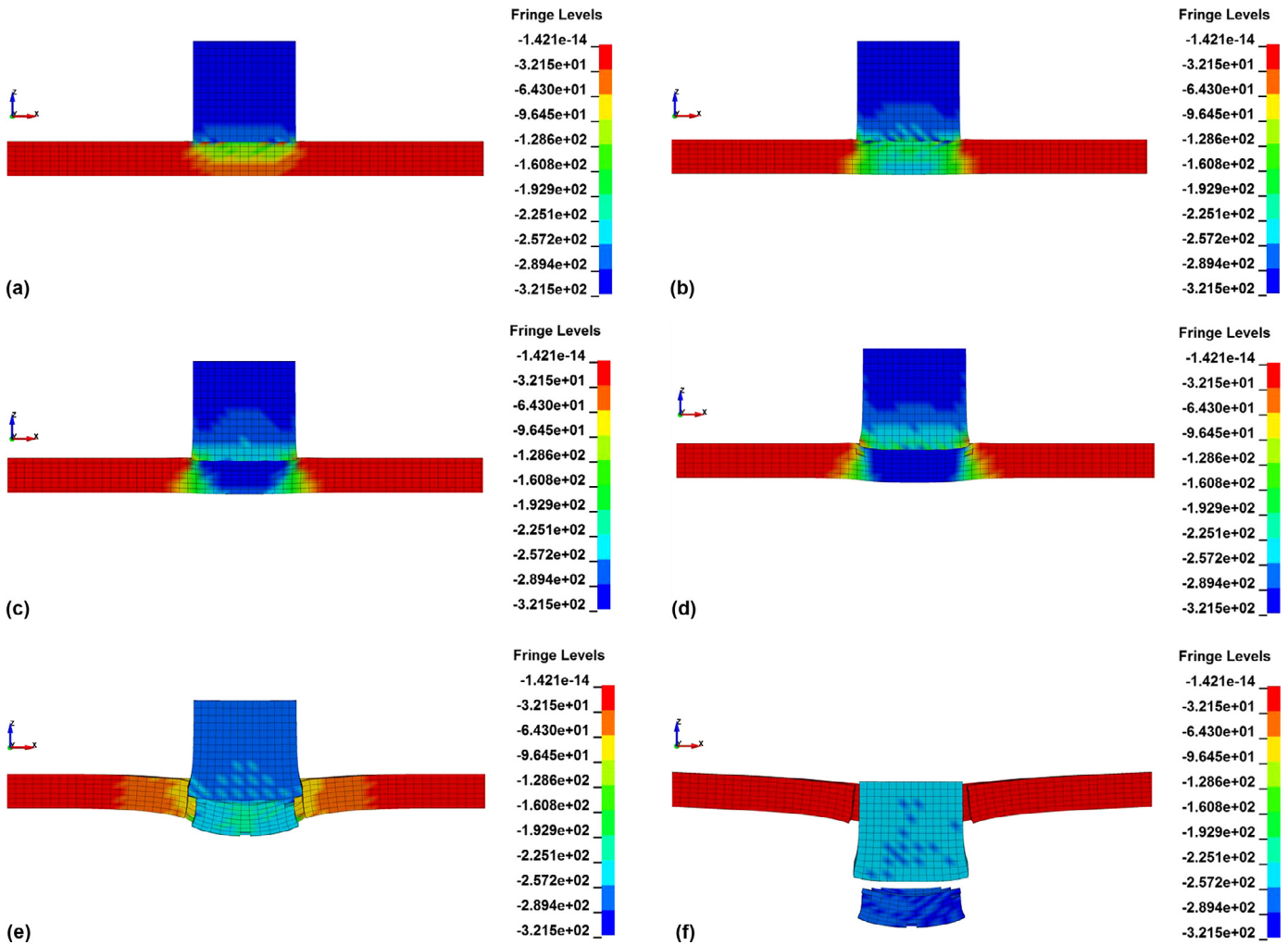
Fig. 25. Velocity in impact direction for 321 m/s impact a) immediately after impact (t = 9.386us), b) when release wave travels from back of target (t = 9.879us), c) when release wave has completely released the target (t = 10.278us) and d) the first elements are being deleted in the shear zone while the velocity of the target below the projectile is still defined by the wave propagation (11.010us), e) when the plug has formed completely (t = 18.193us) and f) when the plug has been ejected and the projectile passed through the target (49.598us).

impact configuration, no clear pressure waves were generated in either projectile or target.

For this failure mode, it was not straightforward to define a reliable measure for the size of the hole in the plate. Measuring hole in the direction of the clamped edges and the direction perpendicular to it results in hole dimensions of roughly 15 mm, with lower and upper bounds of 10 and 20 mm. The simulations predict similar dimensions of approximately 15 mm. The dishing of the plate

Fig. 26. High speed image of corner impact showing a) triangular fragment and b) petalling.
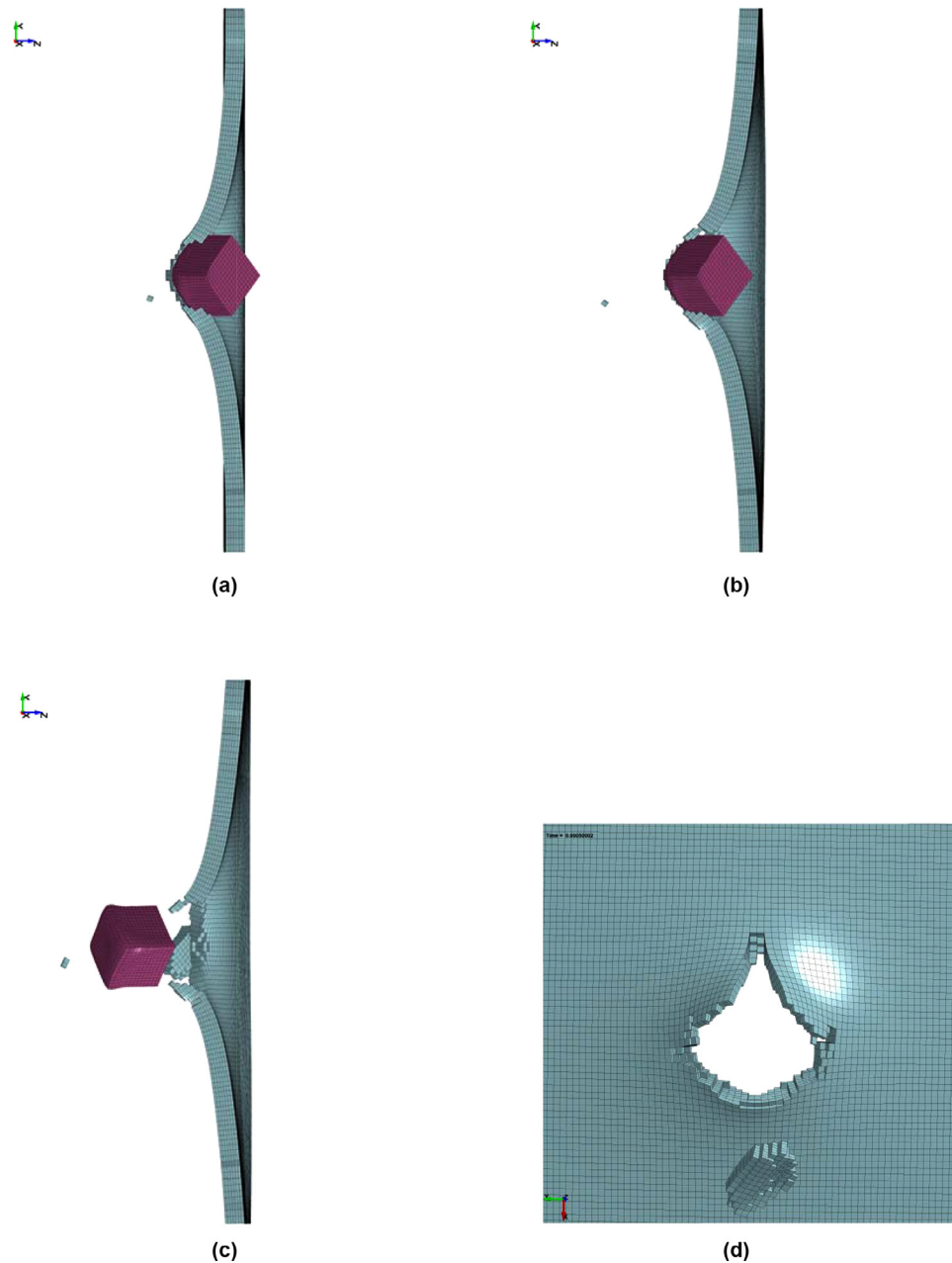
(a)

(b)

(c)

(d)

Fig. 27. Corner Impact penetration mechanism: simulation result.

presented in Fig. 29, is higher than the other impact configurations. The maximum out of plane deflection decreases slightly with increasing impact speed (see Fig. 29). The deflection at 264 m/s is 4.6 mm and at 325 m/s 4.4 mm, with the simulations predicting similar deflections of 5.1 and 3.9 mm respectively.

Since the amount of dishing does not change significantly, the increase in energy absorbed with increasing velocity (see Figs. 5 and 30) is due to more energy being absorbed in local deformation, which is visible in Fig. 28.

5. Discussion

In this section, two aspects of the results presented in the previous paragraphs are analysed in more detail. These two aspects are the differences in ballistic limit and the differences in residual velocities for the impact configurations studied. One

interesting point is that although the edge impact configuration results in the lowest ballistic limit, the face impact configuration generally results in higher residual velocities despite having a higher ballistic limit.

In order to explain the difference in ballistic limit, one can consider the effect of the different projectile nose area for these three impact configurations. This is similar to the analysis by Rusinek [14] who showed that the velocity lost by conical nosed projectiles is proportional to the square root of the projectile diameter (or projectile nose area), and in that case, the curves of velocity lost per unit area as a function of impact speed for different projectile diameters collapse on to one single curve. Fig. 31 shows the velocity lost per unit area versus impact velocity for the three impact configurations studied in this paper. It is clear the curves do not collapse on to one single curve and therefore, the difference in ballistic limit observed cannot be attributed solely to the differences in projectile nose area. This
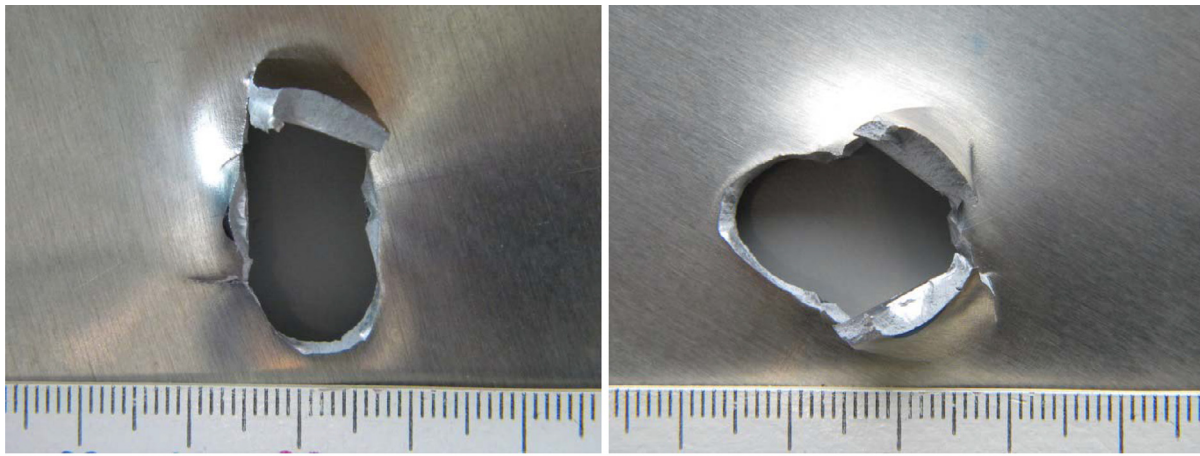
Fig. 28. Deformed state after corner impact at a) 264 m/s and b) 325 m/s.

means that the differences in penetration mechanism of each impact configuration also play a role.

5.1. Ballistic limit

Figs. 32 and 33 show a comparison of the local and global target deformations when impacted just above their ballistic limit.
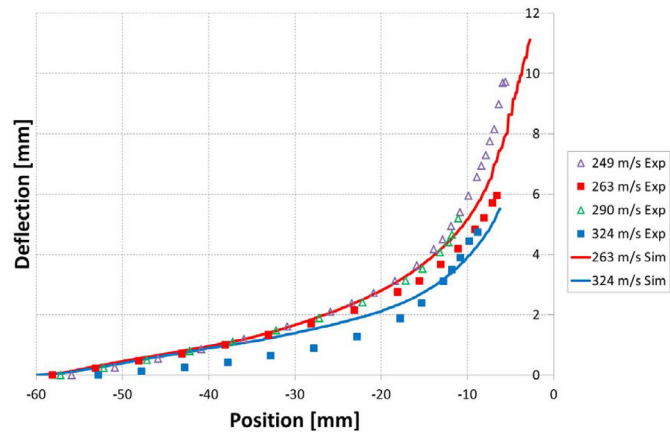

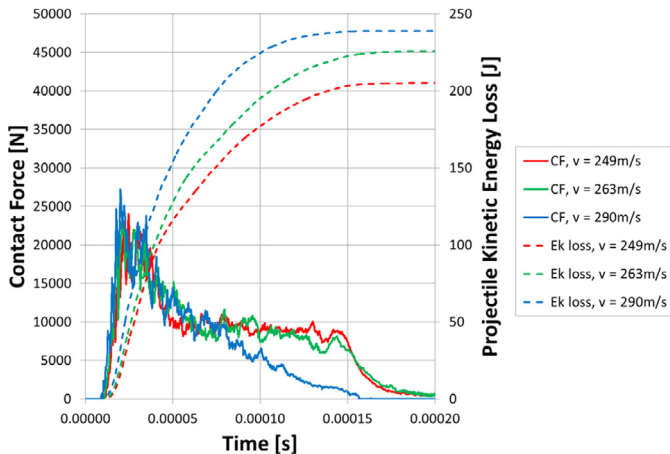**Fig. 29.** Measured and simulated target deflections for corner impact.

Fig. 30. Corner impact contact force (CF) and projectile kinetic energy loss (Ek loss) as a function of time; the 249 m/s impact is below the ballistic limit, the 263 m/s and 290 m/s impacts are above the ballistic limit.

A key observation presented in Fig. 5 for the edge and corner impact configurations is that the energy loss by the projectile continues to increase above the ballistic limit, while for the face impact it decreases after the ballistic limit. As explained earlier, this is due to the momentum transfer from the projectile to the target, which in turn is related to the propagation of the pressure wave generated by the impact.

Fig. 34 shows a comparison of the contact force and the projectile kinetic energy loss time histories of the three cube impact configurations at 215 m/s. This impact velocity is just above the ballistic limit for the edge impact configuration. It can be seen that the contact force time for the corner impact configuration is of similar shape to the edge impact configuration, but the contact force is between 3000 N to 4000 N higher. For the face impact configuration, the high initial peak is followed by a 0.03 ms period where the contact force is much higher (around 15,000 N) than the edge impact.

Considering the impact energy absorption, Fig. 34 demonstrates that the corner impact results in the most gradual, whilst the face impact results in the fastest reduction in projectile kinetic energy, with the edge impact configuration lying somewhere in between. This can be explained by the gradual increase in contact area for the corner and edge impact configurations, while for a face impact, the contact area does not change over time. At this impact speed, the face impact configuration does not result in any perforation, hence the energy absorbed will result in dishing deformation. For both edge and corner impact configurations, the simulations predict that perforation first occurs around 25 μs (this is at time 35 μs in Fig. 34)
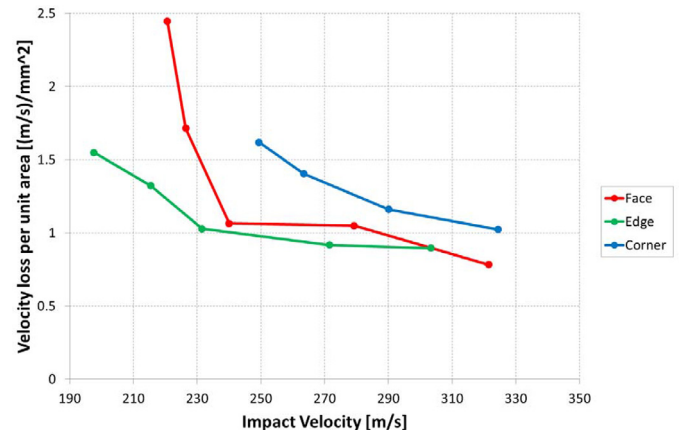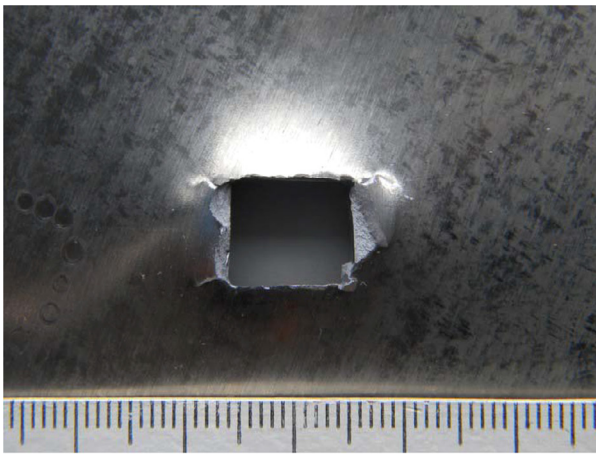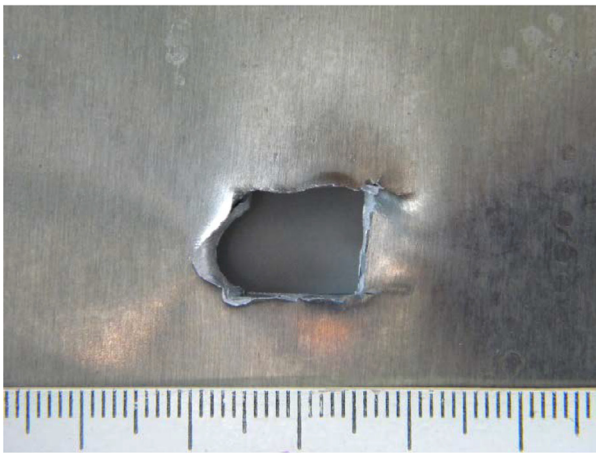

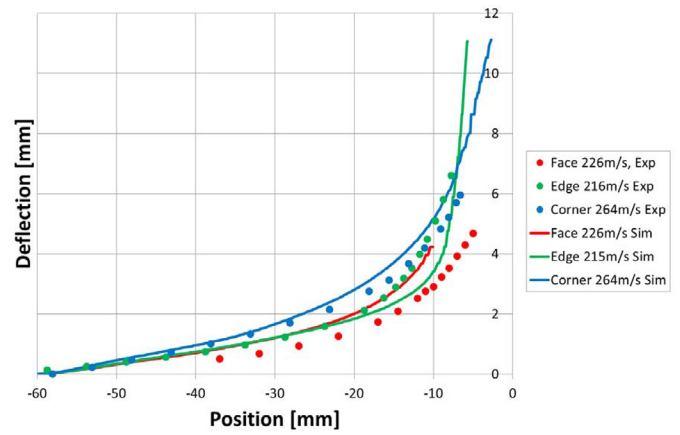**Fig. 31.** Velocity loss per unit projectile area versus impact velocity.

(a)

(b)

(c)

Fig. 32. Local deformations near the ballistic limit: a) face, b) edge, c) corner impact configuration.

Fig. 33. Global deformations near the ballistic limit.
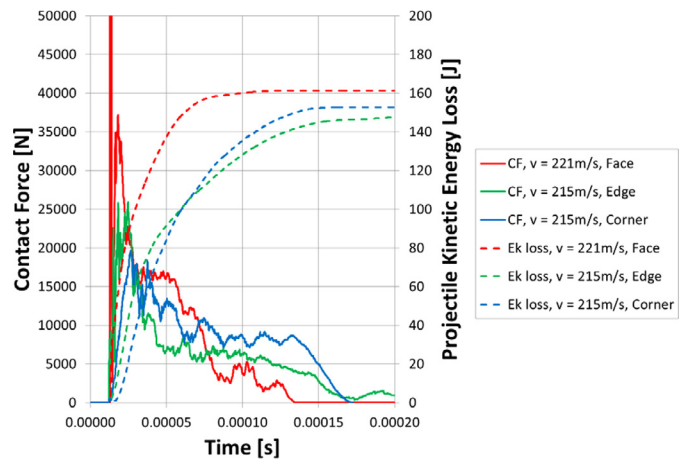
Fig. 34. Contact force (CF) and projectile kinetic energy loss (Ek loss) as a function of time for impact velocity around 215 m/s.

Fig. 35. Contact force (CF) and projectile kinetic energy loss (Ek loss) as a function of time for impact velocity near ballistic limit.

after initial contact. It is clear from the contact force time histories that after this point, it requires less energy to develop the initial perforation into complete penetration for the edge configuration.
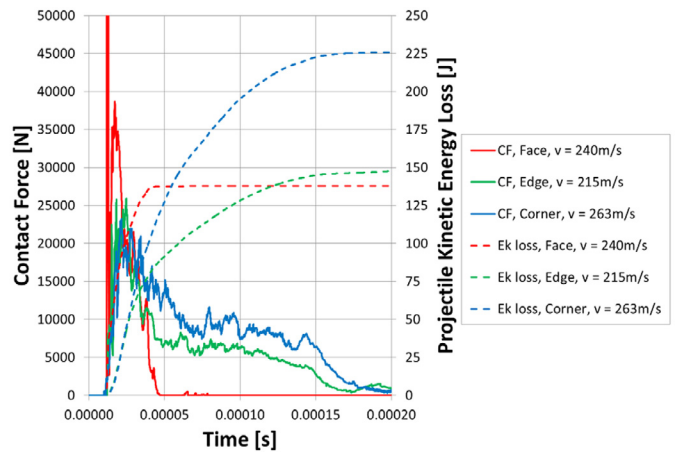
If one compares the contact force and projectile kinetic energy loss time histories of the three cube impact configurations for an impact velocity just above their respective ballistic limits (see Fig. 35), one observes a notable change for the face impact configuration. The contact time reduces to about 25 μs, after which time, the
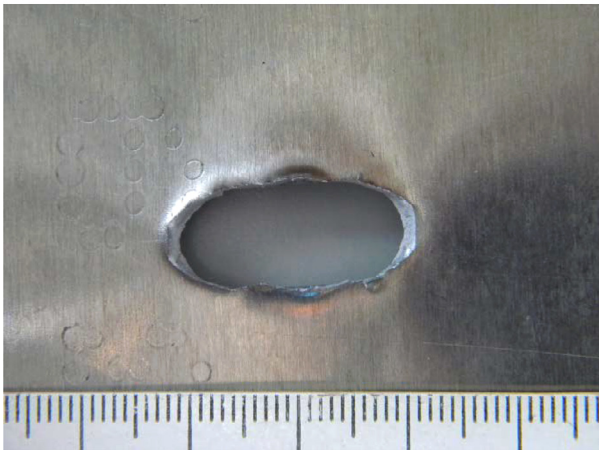
plug is formed completely, penetration has occurred and the energy absorbed by the target reduces also.

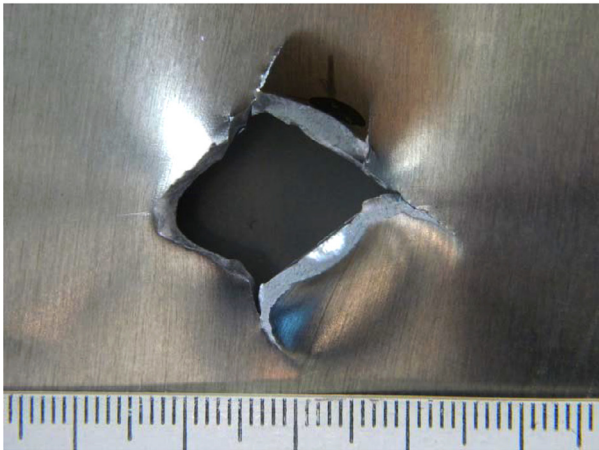### 5.2. Residual velocity

The local and global deformations for the three impact configurations for an impact velocity in the region of 275 m/s are shown in
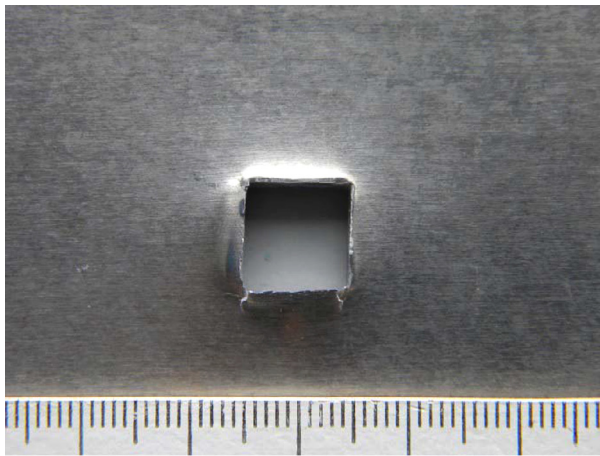
(a)

(b)

(c)

Fig. 36. Local deformations for impact velocity of approximately 275 m/s: a) face, b) edge, c) corner.

Figs. 36 and 12 respectively. The residual velocity at this speed is lowest for the corner impact at 49 m/s. The edge impact has a residual velocity of 156 m/s and the highest residual velocity is for the face impact configuration (188 m/s). Despite the edge impact having a lower ballistic limit than the face impact, for impact velocities well above the ballistic limit, the target absorbs more energy during an edge impact than for a face impact configuration. This can be explained by considering the local and global post impact target deformations and the contact force time histories (Fig. 37). It can be
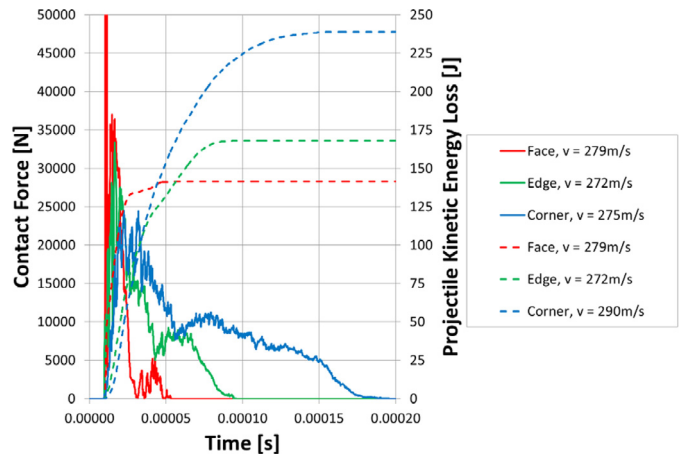
Fig. 37. Contact forces (CF) and projectile kinetic energy loss (Ek loss) for impacts around 275 m/s.

seen in Fig. 36 that the deformation (plug formation) in the impact area for the face impact is almost identical to the deformation at the ballistic limit. For the edge impact, the petals break off completely at higher impact velocities and the hole in the target increases from 9.8 mm by 10 mm to 9.8 mm by 21 mm. The amount of dishing remains relatively constant for the edge impact configuration, while for the face impact, it reduces with increasing impact velocity. These two phenomena explain why at higher impact velocities, the energy absorbed by the target for the face impact decreases and increases for an edge impact. This is confirmed by the plot of projectile kinetic energy loss as a function of impact speed in Fig. 5.

6. Conclusion

In this paper, the response of 3.175 mm thick AA2024-T351 sheets for three impact configurations was determined through a series of impact experiments and simulations. The three configurations consisted of a cubical projectile which was oriented such that it impacted the target with either face, edge or corner orientations.

The results show that the orientation of a cube shaped projectile has a significant effect on the ballistic limit of a 3.175 mm thick AA2024-T351 sheet. The lowest ballistic limit (202 m/s) was observed for an edge on impact, while the highest ballistic limit was observed for a corner impact (254 m/s), i.e. a difference of 25%. A face impact results in a ballistic limit of 223 m/s. The reason for this difference is due to the different way momentum is transferred from the projectile to the target, which results in different failure mechanisms. The face impact configuration results in the target absorbing the least amount of energy above the ballistic limit, resulting in higher residual projectile velocities.

References

[1] Woodward RL. The penetration of metal targets by conical projectiles. Int J Mech Sci 1978;20:349–59.

[2] Woodward RL. The interrelation of failure modes observed in the penetration of metallic targets. Int J Impact Eng 1984;2(2):121–9.

[3] Rosenberg Z, Dekel E. Revisiting the perforation of ductile plates by sharp-nosed rigid projectiles. Int J Solids Struct 2010;47(22-23):3022−33.

[4] Tiwari G, Iqbal MA, Gupta PK, Gupta NK. The ballistic resistance of thin aluminium plates with varying degrees of fixity along the circumference. Int J Impact Eng 2014;74(December):46−56.

[5] Iqbal MA, Khan SH, Ansari R, Gupta NK. Experimental and numerical studies of double-nosed projectile impact on aluminum plates. Int J Impact Eng 2013;54:232−45.

[6] Iqbal MA, Gupta G, Diwakar A, Gupta NK. Effect of projectile nose shape on the ballistic resistance of ductile targets. Eur J Mech A/Solids 2010;29(4):683−94.

[7] Gupta NK, Iqbal MA, Sekhon GS. Effect of projectile nose shape, impact velocity and target thickness on the deformation behavior of layered plates. Int J Impact Eng 2008;35(1):37−60.

[8] Gupta NK, Iqbal MA, Sekhon GS. Effect of projectile nose shape, impact velocity and target thickness on deformation behavior of aluminum plates. Int J Solids Struct 2007;44(10):3411−39.

[9] Iqbal MA, Tiwari G, Gupta PK, Bhargava P. Ballistic performance and energy absorption characteristics of thin aluminium plates. Int J Impact Eng 2015;77:1−15.

[10] Iqbal MA, Diwakar A, Rajput A, Gupta NK. Influence of projectile shape and incidence angle on the ballistic limit and failure mechanism of thick steel plates. Theor Appl Fract Mech 2012;62(1):40−53.

[11] Senthil K, Iqbal MA. Effect of projectile diameter on ballistic resistance and failure mechanism of single and layered aluminum plates. Theor Appl Fract Mech 2013;66-67:53−64.

[12] Rodríguez-Millán M, Vaz-Romero A, Rusinek A, Rodríguez-Martínez JA, Arias A. Experimental study on the perforation process of 5754-H111 and 6082-T6 aluminium plates subjected to normal impact by conical, hemispherical and blunt projectiles. Exp Mech 2014;54(5):729−42.

[13] Jankowiak T, Rusinek A, Wood P. A numerical analysis of the dynamic behaviour of sheet steel perforated by a conical projectile under ballistic conditions. Finite Elem Anal Des 2013;65:39−49.

[14] Rusinek A, Rodríguez-Martínez JA, Arias A, Klepaczko JR, López-Puente J. Influence of conical projectile diameter on perpendicular impact of thin steel plate. Eng Fract Mech 2008;75(10):2946−67.

[15] Arias A, Rodríguez-Martínez JA, Rusinek A. Numerical simulations of impact behaviour of thin steel plates subjected to cylindrical, conical and hemispherical non-deformable projectiles. Eng Fract Mech 2008;75(6):1635−56.

[16] Kpenyigba KM, Jankowiak T, Rusinek A, Pesci R, Wang B. Effect of projectile nose shape on ballistic resistance of interstitial-free steel sheets. Int J Impact Eng 2015;79(May):83−94.

[17] Børvik T, Hopperstad OS, Pedersen KO. Quasi-brittle fracture during structural impact of AA7075-T651 aluminium plates. Int J Impact Eng 2010;37(5):537−51.

[18] Børvik T, Dey S, Clausen AH. Perforation resistance of five different high-strength steel plates subjected to small-arms projectiles. Int J Impact Eng 2009;36(7):948−64.

[19] Børvik T, Clausen AH, Eriksson M, Berstad T, Hopperstad OS, Langseth M. Experimental and numerical study on the perforation of AA6005-T6 panels. Int J Impact Eng 2006;32(1-4):35−64.

[20] Raguraman M, Jagadeesh G, Deb A, Barton DC. Experimental and numerical investigation of the behavior of aluminium plates upon ballistic impact. Exp Tech 2010;34(6):49−60.

[21] Jordan JB, Naito CJ. An experimental investigation of the effect of nose shape on fragments penetrating GFRP. Int J Impact Eng 2014;63:63−71.

[22] Yunfei D, Wei Z, Yonggang Y, Lizhong S, Gang W. Experimental investigation on the ballistic performance of double-layered plates subjected to impact by projectile of high strength. Int J Impact Eng 2014;70:38−49.

[23] Yunfei D, Wei Z, Yonggang Y, Gang W. The ballistic performance of metal plates subjected to impact by projectiles of different strength. Mater Des 2014;58:305−15.

[24] Yunfei D, Wei Z, Guanghui Q, Gang W, Yonggang Y, Peng H. The ballistic performance of metal plates subjected to impact by blunt-nosed projectiles of different strength. Mater Des 2014;54:1056−67.

[25] Wei Z, Yunfei D, Sheng CZ, Gang W. Experimental investigation on the ballistic performance of monolithic and layered metal plates subjected to impact by blunt rigid projectiles. Int J Impact Eng 2012;49:115−29.

[26] Deng Y-F, Zhang W, Cao Z-S. Experimental investigation on the ballistic performance of 45 steel metal plates subjected to impact by hemispherical-nosed projectiles. Gaoya Wuli Xuebao/Chinese J High Pressure Phys 2013;27(6):915−20.

[27] Deng Y, Zhang W, Cao Z. Experimental investigation on the ballistic resistance of monolithic and multi-layered plates against hemispherical-nosed projectiles impact. Mater Des 2012;41:266−81.

[28] Woodward RL, Cimpoeru SJ. A study of the perforation of aluminium laminate targets. Int J Impact Eng 1998;21(3):117−31.

[29] Erice B, Pérez-Martín MJ, Gálvez F. An experimental and numerical study of ductile failure under quasi-static and impact loadings of Inconel 718 nickel-base superalloy. Int J Impact Eng 2014;69:11−24.

[30] Seidt JD, Michael Pereira J, Gilat A, Revilock DM, Nandwana K. Ballistic impact of anisotropic 2024 aluminum sheet and plate. Int J Impact Eng 2013;62:27−34.

[31] Wang J, Zhou N. Damage mechanism and anti-penetration performance of explosively welded plates impacted by projectiles with different shapes. Mater Des 2013;49:966−73.

[32] Ulven C, Vaidya UK, Hosur MV. Effect of projectile shape during ballistic perforation of VARTM carbon/epoxy composite panels. Compos Struct 2003;61(1-2):143−50.

[33] Tan VBC, Lim CT, Cheong CH. Perforation of high-strength fabric by projectiles of different geometry. Int J Impact Eng 2003;28(2):207−22.

[34] Recht RF, Ipson TW. Ballistic perforation dynamics. J Appl Mech 1963;30:384−90.

[35] LS-DYNA. Keyword user's manual, Vol I-II. Livermore Software Technology Corporation (LSTC); 2013.

[36] Hypermesh. accessed online 15 http://www.altairhyperworks.com/; December 2015 accessed online 15 .

[37] Buyuk M, Loikkanen M, Kan CS. A computational and experimental analysis of ballistic impact to sheet metal aircraft structures. 5th Europe LS-DYNA users conference; 2005.

[38] Barlat F, Lege DJ, Brem JC. A six-component yield function for anisotropic materials. Int J Plast 1991;7:693−712.

[39] Azorin Albero A. Numerical study of the impact response and ballistic limit of AA2024 friction stir welded aircraft panels MSc thesis. Cranfield, UK: Cranfield University; 2014.

[40] Kelly S, Johnson G. Statistical testing of aircraft materials for transport airplane rotor burst fragment shielding. U.S. Department of Transportation Federal Aviation Administration Report DOT/FAA/AR-06/9; May 2006.

[41] Backman ME, Goldsmith W. The mechanics of penetration of projectiles into targets. Int J Eng Sci 1978;16(1):1−99.